

# Boosting Sodium Storage of Titanium Oxide through Homojunction Design

Maiji Zhang,<sup>[a]</sup> Zhenzhu Wang,<sup>[a]</sup> Jiangfeng Ni,<sup>\*[a, b]</sup> and Liang Li<sup>\*[a]</sup>

Sodium-ion batteries are regarded as the energy storage of choice for large-scale applications due to their ample resource and low cost. However, their practical application has been largely retarded by the lack of efficient and stable anodes capable of storing a large amount of  $\text{Na}^+$  ions reversibly. In this work, we introduce the concept of homojunction into the design of sodium anodes by growing  $\text{TiO}_2$  nanowires composed of both anatase and bronze intimately interwoven. The interplay between the two phases brings abundant boundaries and

interfaces, which drastically increase the storage sites and facilitate the transport of  $\text{Na}^+$  ions. As a result, it reveals robust  $\text{Na}^+$  storage, affording a capability of  $140 \text{ mAh g}^{-1}$  at a high rate of 20 C and retaining 85% of the initial capacity after 3000 cycles at 5 C. Furthermore, the practice of  $\text{TiO}_2$  homojunction has been explored by pairing it with  $\text{Na}_3\text{V}_2(\text{PO}_4)_2\text{O}_2\text{F}$  cathode, thereby demonstrating the potential of designing homojunction as a promising materials strategy in rechargeable batteries.

## Introduction

Sodium-ion batteries (SIBs) have become a strong competitor for next-generation energy storage batteries due to their abundant resources and low cost.<sup>[1–4]</sup> The development of anode materials with high capacity, robust rate, and long lifespan is one of the keys to promoting the development of SIBs.<sup>[5–7]</sup> As a promising anode material, titanium oxide ( $\text{TiO}_2$ ) has attracted extensive attention because of its nontoxicity, potentially high capacity, and suitable working voltage (0.7 V vs.  $\text{Na}/\text{Na}^+$ ).<sup>[8,9]</sup> However,  $\text{TiO}_2$  is a typical semiconductor with a large band gap (~3.2 eV), resulting in poor electrical conduction.<sup>[10,11]</sup>

To improve the electrochemical performance of  $\text{TiO}_2$ , several strategies have been reported such as constructing nanostructures,<sup>[12,13]</sup> incorporating carbon matrix,<sup>[14–16]</sup> introducing lattice defects,<sup>[17,18]</sup> and doping of exotic elements.<sup>[19,20]</sup> These strategies help to mitigate the conduction issue, thus raising the electrochemical  $\text{Na}^+$  storage performance. Despite their effectiveness, these strategies face some new challenges in practice. For instance, nanostructures usually show a low tap density,<sup>[21]</sup> while carbon coating only addresses the interparticle conduction issue.<sup>[22,23]</sup> Previously, our group has architected free-standing nanoarrays of  $\text{TiO}_2$ , enabling a remarkable

improvement in electrochemical performance.<sup>[24,25]</sup> This is because these arrays feature a large accessible surface, short ion-transport path, and robust electrical connection between electrode and substrate.<sup>[2,26,27]</sup> Nonetheless, the massive fabrication of  $\text{TiO}_2$  architectures remains a grand challenge.

Another solution to this issue is to design a heterostructure of  $\text{TiO}_2$  such as  $\text{TiO}_2@\text{SnS}_2$ <sup>[28]</sup> and  $\text{TiO}_2@\text{SnO}_2$ .<sup>[29]</sup> In the heterostructure, an electric field is often built in the interphase due to the difference in Fermi level between two components. The built-in electric field could speed the transport of charge carriers.<sup>[30,31]</sup> However, heterostructures have to address the issues of lattice mismatch, lattice distortion, and phase separation.<sup>[32,33]</sup> As a result, many  $\text{TiO}_2$  heterostructures still exhibit insufficient capacity levels and poor rate performance.

An alternative solution is to design homojunction to enhance the electrochemical  $\text{Na}^+$  storage in  $\text{TiO}_2$ . A homojunction refers to a semiconductor interface that shares a similar semiconductor material but has a different structure or doping level.<sup>[34]</sup> Homojunction features rich phase boundaries that offer freeway for rapid ion transport and active sites for  $\text{Na}^+$  storage.<sup>[33,35,36]</sup> In recent years, homojunction design has been extensively used in fields such as photoelectrocatalysis,<sup>[37,38]</sup> and solar cells.<sup>[39,40]</sup> However, its exploration in rechargeable batteries is relatively rare.

Herein, we propose the design of  $\text{TiO}_2$  homojunction of anatase and bronze (hereafter designated  $\text{TiO}_2(\text{A/B})$ ) to boost the electrochemical  $\text{Na}^+$  storage in  $\text{TiO}_2$ .  $\text{TiO}_2$  exhibits versatile crystal structures; among them, anatase and bronze are two more exciting phases suitable for  $\text{Na}^+$  intercalation and storage because of their open structure and multiple diffusion channels.<sup>[8,41]</sup> When the two phases are brought to contact, the charge redistribution will take place in the homojunction deriving from the Fermi level difference and result in a driving force to accelerate the ion diffusion.<sup>[42,43]</sup> Meanwhile, the rich interfaces between them will provide more active sites for ion storage.<sup>[35,44]</sup> Significantly, the  $\text{TiO}_2$  homojunction exhibits an excellent rate capability of  $140 \text{ mAh g}^{-1}$  at 20 C (1 C =

[a] M. Zhang, Z. Wang, Prof. J. Ni, Prof. L. Li  
School of Physical Science and Technology, Center for Energy Conversion Materials & Physics (CECMP)  
Jiangsu Key Laboratory of Thin Films  
Soochow University  
215006 Suzhou, China  
E-mail: jeffni@suda.edu.cn  
li@suda.edu.cn

[b] Prof. J. Ni  
Light Industry Institute of Electrochemical Power Sources  
215699 Suzhou, China

Supporting information for this article is available on the WWW under  
<https://doi.org/10.1002/batt.202200264>

An invited contribution to a Special Collection on IV Symposium on Advanced Energy Storage

$335 \text{ mA g}^{-1}$ ) and sustains 85% of the capacity after 3000 cycles at 5 C, outperforming the single-phase and many recently reported  $\text{TiO}_2$  anodes. In addition, the full cell of  $\text{TiO}_2(\text{A/B})/\text//\text{Na}_3\text{V}_2(\text{PO}_4)_2\text{F}$  realizes an energy density of  $160 \text{ Wh kg}^{-1}$ , thereby demonstrating its great potential in practical sodium batteries for renewable and grid energy.

## Results and Discussion

$\text{TiO}_2$  homojunction can be prepared through a two-step process, as illustrated in Figure 1(a). In the first step, commercial  $\text{TiO}_2$  powder was hydrothermally treated with  $\text{NaOH}$  solution at  $160^\circ\text{C}$  for 24 h. Upon this process,  $\text{Ti}-\text{O}-\text{Ti}$  bonds would be broken and  $\text{Na}_2\text{Ti}_3\text{O}_7$  nanowires were generated.<sup>[45]</sup> Afterward, these nanowires were immersed in an acidic solution for ion exchange, giving rise to  $\text{H}_2\text{Ti}_3\text{O}_7$  nanowires (Figure S1). In the second step, as-prepared  $\text{H}_2\text{Ti}_3\text{O}_7$  nanowires were vacuum dried and then annealed at a certain temperature ( $500^\circ\text{C}$ ,  $600^\circ\text{C}$ , and  $700^\circ\text{C}$ ) for 4 hours to give the final product. Interestingly,  $\text{TiO}_2$  homojunction ( $\text{TiO}_2(\text{A/B})$ ) can be fabricated at a temperature of  $600^\circ\text{C}$ . At heating temperatures of  $500$  and  $700^\circ\text{C}$ , the final product is dominated by  $\text{TiO}_2$  bronze ( $\text{TiO}_2(\text{B})$ ) and anatase ( $\text{TiO}_2(\text{A})$ ), respectively. Here we focus on the  $\text{TiO}_2(\text{A/B})$  product, which was characterized by scanning electron microscopy (SEM) and transmission electron microscopy (TEM). Clearly,  $\text{TiO}_2(\text{A/B})$  is composed of uniform nanowires,  $\sim 3 \mu\text{m}$  in length and  $\sim 100 \text{ nm}$  in diameter (Figure 1b and c). The SEM images of  $\text{TiO}_2(\text{A})$  and  $\text{TiO}_2(\text{B})$  are also showed in Figure S2. High-resolution TEM imaging reveals two distinct phases in  $\text{TiO}_2(\text{A/B})$  (Figures 1d and S3). The  $d$ -spacings of  $0.298$  and  $0.300 \text{ nm}$  correspond to the  $(111)$  and  $(40\bar{1})$  planes of the bronze phase, respectively. Meanwhile, the  $d$ -spacing of  $0.189 \text{ nm}$  well agrees with the distance of the  $(200)$  plane of anatase. The interwoven phases in a single nanowire afford abundant interphase and boundaries for  $\text{Na}^+$  transport and accommodation.<sup>[44,46]</sup> Hence,

it is expected that  $\text{TiO}_2(\text{A/B})$  would exhibit improved electrochemical performance for  $\text{Na}^+$  storage.

The temperature-dependent structure evolution was studied by X-ray diffraction (XRD) and Raman spectroscopy. As Figure 2(a) shows, different crystal structures of  $\text{TiO}_2$  will be produced at varied annealing temperatures. The product is primarily composed of the bronze phase at  $500^\circ\text{C}$ , and of anatase at  $700^\circ\text{C}$ . At an intermediate temperature of  $600^\circ\text{C}$ , both bronze and anatase are present. If we extend the heating duration at  $600^\circ\text{C}$ , more bronze will transform to anatase (Figure S4a). This result suggests that  $600^\circ\text{C}$  might be a critical temperature where the phase evolution between bronze and anatase can be realized. This trend of structure evolution is also verified by Raman spectroscopy (Figures 2b and S4b). Importantly, the vibration bands at  $123$  and  $144 \text{ cm}^{-1}$  are the characteristic band of bronze and anatase, respectively. Based on this Raman feature, the contents of anatase in the three products of  $\text{TiO}_2(\text{B})$ ,  $\text{TiO}_2(\text{A/B})$ , and  $\text{TiO}_2(\text{A})$  are identified as 7%, 24%, and 100%, respectively (see details in Figures S4c, d and S5).<sup>[47]</sup> In addition, the chemical states of  $\text{TiO}_2(\text{A/B})$  are verified by X-ray photoelectron spectroscopy (XPS, Figures S6, and 2c, d). The core-level spectrum of  $\text{Ti} 2\text{p}$  displays two strong peaks at  $458.4 \text{ eV}$  and  $464.1 \text{ eV}$ , confirming the presence of  $\text{Ti}^{4+}$ .<sup>[25]</sup> The peaks of  $529.7 \text{ eV}$  and  $531.1 \text{ eV}$  for  $\text{O} 1\text{s}$  can be assigned to  $\text{O}-\text{Ti}$  and  $\text{OH}-\text{Ti}$ , respectively.<sup>[48]</sup>

2032 coin cells were assembled to illustrate the effectiveness of this homojunction design. Figure 3(a) shows cyclic voltammetry (CV) curves of  $\text{TiO}_2(\text{A/B})$  electrodes measured in the voltage range of  $0.1$  to  $2.5 \text{ V}$  at the sweep rate of  $0.2 \text{ mV s}^{-1}$ . The first cathodic scan shows a large irreversible peak in the range of  $0.6$ – $1.0 \text{ V}$ , which can be attributed to the formation of solid-electrolyte interphase (SEI).<sup>[15,16,49]</sup> In the following cycles,  $\text{TiO}_2(\text{A/B})$  shows a pair of broad peaks at  $0.80$ / $0.82 \text{ V}$ , representing the charge transfer between  $\text{Ti}^{4+}$  and  $\text{Ti}^{3+}$  accompanied by the intercalation and deintercalation of  $\text{Na}^+$  ions. Figure 3(b) exhibits the galvanostatic charge and dis-

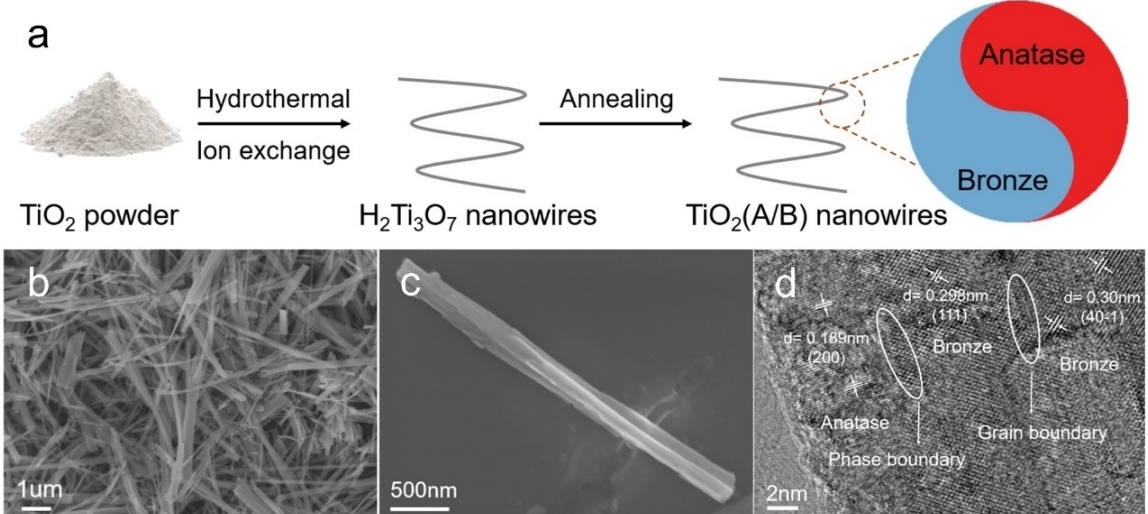


**Figure 1.** Synthesis and characterization of  $\text{TiO}_2(\text{A/B})$  nanowires. a) Schematic illustrating the growth of  $\text{TiO}_2(\text{A/B})$  nanowires. b) and c) SEM images of  $\text{TiO}_2(\text{A/B})$ . d) TEM image of  $\text{TiO}_2(\text{A/B})$ , showing the presence of rich phase boundaries.

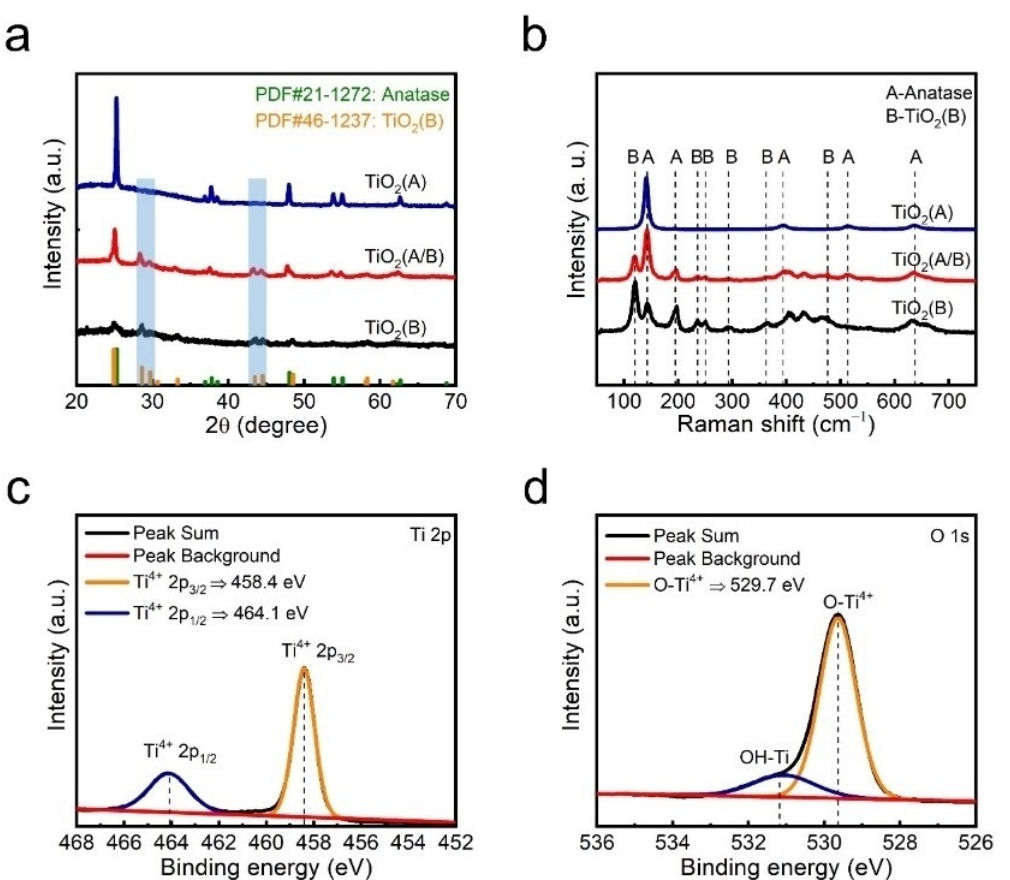


**Figure 2.** Structure and chemical composition of  $\text{TiO}_2$ (A/B). a) XRD patterns and b) Raman spectra of three  $\text{TiO}_2$  nanowire products. Core-level XPS spectra of c) Ti 2p and d) O 1s of  $\text{TiO}_2$ (A/B).

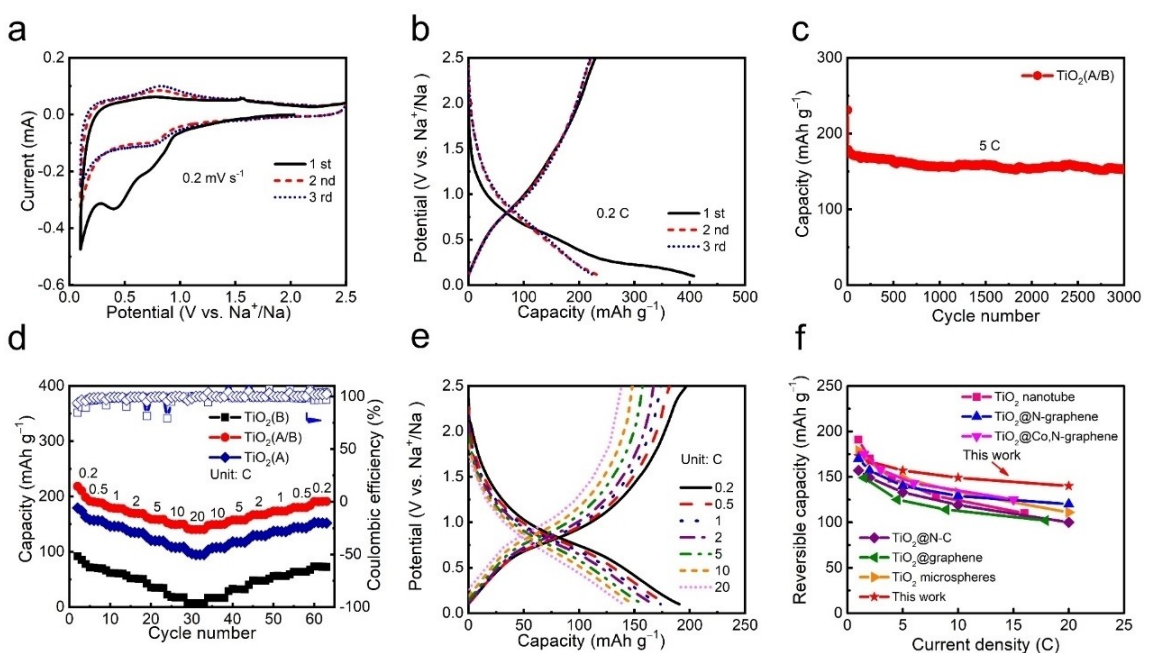


**Figure 3.** Electrochemical  $\text{Na}^+$  storage performance of  $\text{TiO}_2$ (A/B). a) Initial CV curves at a rate of  $0.2 \text{ mV s}^{-1}$ . b) Initial galvanostatic curves. c) Cycling performance of  $\text{TiO}_2$ (A/B). d) Comparison of rate capability of three  $\text{TiO}_2$  nanowire products. e) Galvanostatic profiles of  $\text{TiO}_2$ (A/B) at various current rates. f) Comparison of rate capability of  $\text{TiO}_2$ (A/B) with recently reported  $\text{TiO}_2$ -based electrodes.

charge curves of  $\text{TiO}_2(\text{A/B})$  at a rate of 0.2 C ( $1 \text{C} = 335 \text{ mA g}^{-1}$ ).  $\text{TiO}_2(\text{A/B})$  delivers a reversible (charge) capacity of  $230 \text{ mAh g}^{-1}$  in the first charge. The initial Coulombic efficiency is 56.2%, as a result of the formation of SEI and irreversible trapping of  $\text{Na}^+$  ions. SEM-EDS is conducted to confirm the irreversible trapping of  $\text{Na}^+$  ions in Figure S7. In the subsequent cycles, the reversible capacity remains unchanged, but the Coulombic efficiency markedly increases to 95% and beyond. Similarly, the Coulombic efficiency of  $\text{TiO}_2(\text{A})$  and  $\text{TiO}_2(\text{B})$  are 53.6% and 33.6%, respectively (Figure S8). The homojunction is electrochemically stable (Figure 3c). At a high rate of 5 C,  $\text{TiO}_2(\text{A/B})$  maintains a capacity of  $162 \text{ mAh g}^{-1}$  after 500 cycles and retains  $152 \text{ mAh g}^{-1}$  after 3000 cycles. The capacity decay is as low as 0.005% per cycle (Figure S9).

For three samples,  $\text{TiO}_2(\text{A})$  is electrochemically active toward  $\text{Na}^+$  while  $\text{TiO}_2(\text{B})$  is almost not. However,  $\text{TiO}_2(\text{A/B})$  exhibits a capacity superior to  $\text{TiO}_2(\text{A})$  although it consists of  $\text{TiO}_2(\text{B})$ . Even with different content of  $\text{TiO}_2(\text{B})$ ,  $\text{TiO}_2(\text{A/B})$  shows accordantly high activity (Figure S10). This result indicates that the design of homojunction brings substantial augment in the capacity, as a direct result of grain and phase boundaries. These boundaries supply not only additional sites for  $\text{Na}^+$  accommodation but also freeway for rapid ion travel.<sup>[35,50,51]</sup> As shown in Figure 3(d and e),  $\text{TiO}_2(\text{A/B})$  affords desodiation capacities of 199, 181, 173, 167, 157, 149, and 140  $\text{mAh g}^{-1}$  at 0.2, 0.5, 1, 2, 5, 10 and 20 C, respectively, which are consistently higher than those of  $\text{TiO}_2(\text{A})$  and  $\text{TiO}_2(\text{B})$ . In addition, such a rate capability is superior to many recently reported  $\text{TiO}_2$  anodes (Figure 3f and Table S1).<sup>[13,16,49,50,52,53]</sup>

To unravel the kinetic feature of  $\text{TiO}_2(\text{A/B})$ , CV scans at various rates have been implemented (Figure 4). Significantly,

when the rate increases from 0.2 to 1.0  $\text{mVs}^{-1}$ , the CV curve reveals a redox pair at 0.80/0.82 V without evident distortion, reflecting vigorous reversibility upon  $\text{Na}^+$  storage. The character reflects a pseudocapacitive behavior for  $\text{Na}^+$  storage, as observed previously,<sup>[24,54,55]</sup> and further enables higher sweep rates up to 50  $\text{mVs}^{-1}$ . To quantitatively assess the kinetic robustness of  $\text{TiO}_2(\text{A/B})$ , we plot the CV peak current ( $i_p$ ) versus scan rate ( $v$ ) logarithmically in Figure 4(c). The slope ( $b$ ) of the fitted line determines the kinetic feature of electrochemical reactions. A  $b$  value of 1 indicates a capacitive process, while a  $b$  value of 0.5 suggests a diffusion-controlled process. As both  $b$  values in the cathodic and anodic processes are greater than 0.9, the sodium storage process can be regarded a pseudocapacitive reaction. Using the Trasatti methodology [Eq. (1)], we can quantitatively determine the capacitive and diffusion-controlled contribution separately.<sup>[56]</sup>

$$Q = Q_s + Q_b = Q_s + kv^{-1/2} \quad (1)$$

where  $Q$ ,  $Q_s$ , and  $Q_b$  are the total charge storage, the surface charge contribution, and the bulk diffusion contribution, respectively. Figure 4(d–f) shows that  $Q_s$  dominates the total capacity in the electrode reaction. The ratio of  $Q_s$  increases from 79.5% at 0.2  $\text{mVs}^{-1}$  to 89.6% at 1.0  $\text{mVs}^{-1}$ , larger than that of  $\text{TiO}_2(\text{B})$  and  $\text{TiO}_2(\text{A})$  (Figure S11). This can be attributed to the rich grain boundaries of  $\text{TiO}_2(\text{A/B})$  that provide a large portion of interphase for  $\text{Na}^+$  storage.

The kinetic feature of  $\text{TiO}_2(\text{A/B})$  is also measured by the galvanostatic intermittent titration technique (GITT) and electrochemical impedance spectroscopy (EIS) (Figure S12).  $\text{TiO}_2(\text{A/B})$  shows a better dynamic behavior in both GITT and

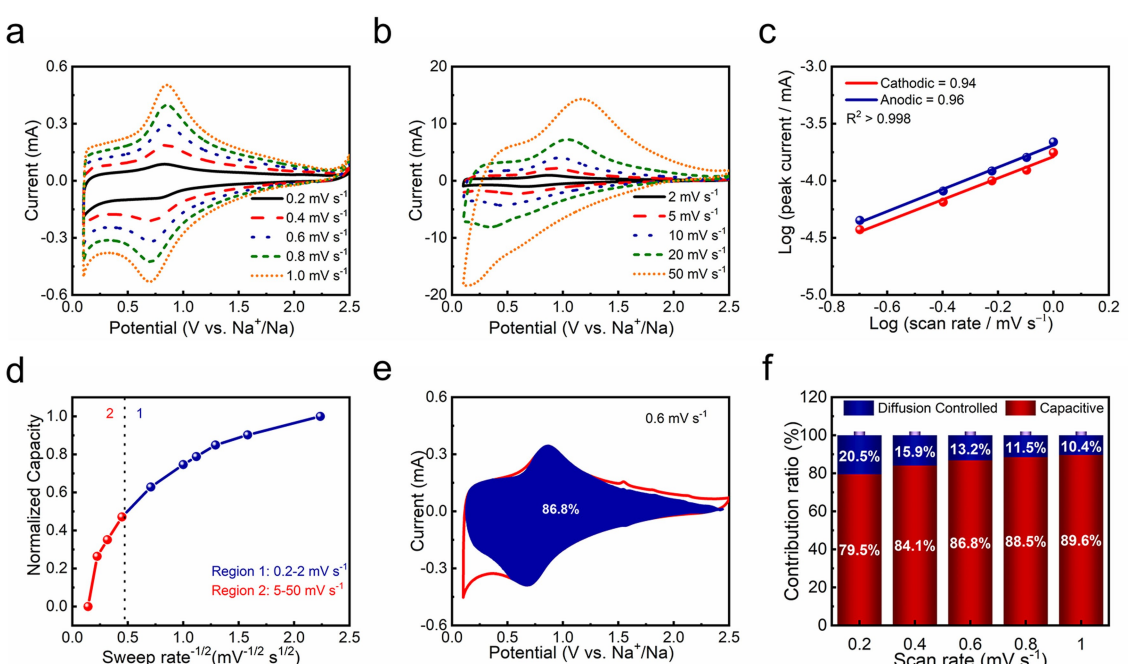


**Figure 4.** Kinetic analysis of  $\text{TiO}_2(\text{A/B})$  by CV tests. CV curves at various sweep rates a) 0.2–1.0  $\text{mVs}^{-1}$  and b) 2.0–50  $\text{mVs}^{-1}$ . c) Relationship between the peak currents and the potential sweep rates. d) The normalized capacity versus the reciprocal square root of the sweep rates. e) Capacitive contribution measured at a sweep rate of 0.6  $\text{mVs}^{-1}$ . f) Ratio of capacitive against the diffusion-controlled capacity at different sweep rates.

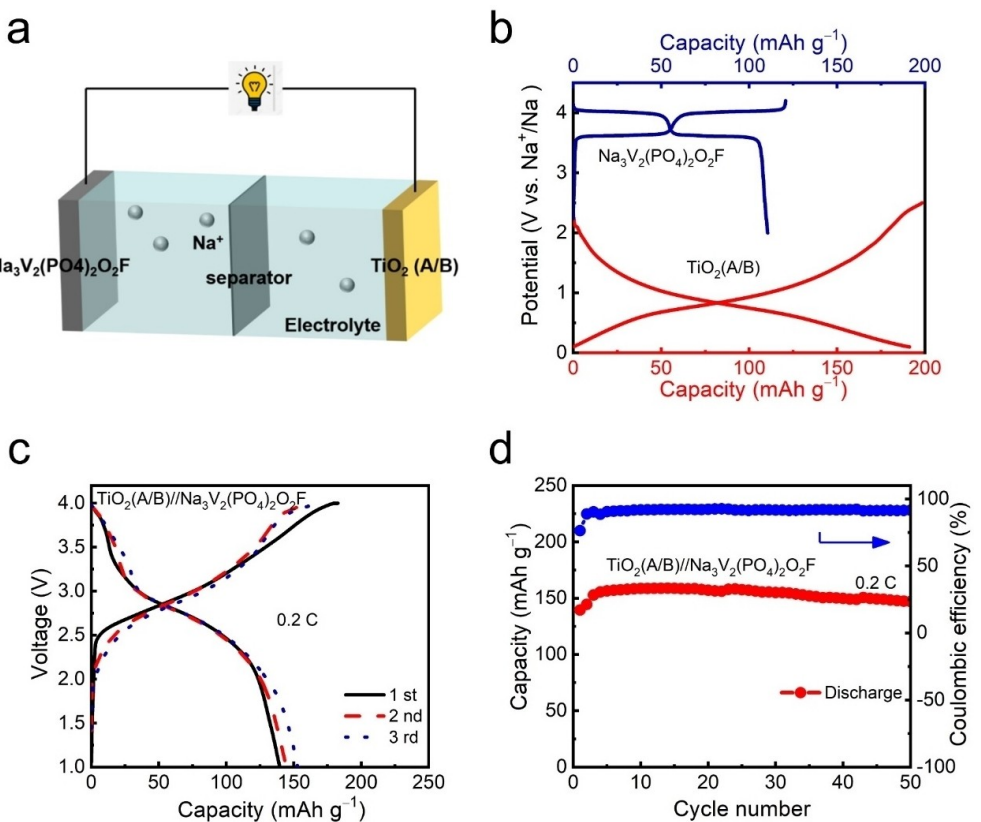


**Figure 5.** Electrochemical performance of TiO<sub>2</sub>(A/B)//Na<sub>3</sub>V<sub>2</sub>(PO<sub>4</sub>)<sub>2</sub>O<sub>2</sub>F full cell. a) A scheme of the full cell. b) Galvanostatic curves of Na<sub>3</sub>V<sub>2</sub>(PO<sub>4</sub>)<sub>2</sub>O<sub>2</sub>F cathode (blue) and TiO<sub>2</sub>(A/B) anode (red) half cells. c) Galvanostatic curves of a full cell for the initial three cycles at 0.2 C. d) Cycling performance of the full cell. The capacity in panels (c, d) is based on the anode.

EIS results, again confirming the efficacy of constructing homojunctions. The improved kinetic feature may result from the rich grain boundaries, which reduce activation barrier and thus accelerate ion transport.<sup>[36]</sup>

The band gaps of three samples are investigated by UV-visible spectroscopy (Figure S13a and b). The samples show similar spectra, with the absorption edge located at 400 nm.<sup>[35,42]</sup> As the Fermi levels of anatase and bronze have differences,<sup>[42,43]</sup> charges will be distributed on both sides of the interface between anatase and bronze, leading to an internal electric field that could accelerate the transport and charge carriers.<sup>[35,36,57]</sup> The conductivity of three samples shown in Figure S13(c) confirms this trend.

To demonstrate the potential of homojunction in practical batteries, TiO<sub>2</sub>(A/B)//Na<sub>3</sub>V<sub>2</sub>(PO<sub>4</sub>)<sub>2</sub>O<sub>2</sub>F full cells were assembled and electrochemically evaluated. Na<sub>3</sub>V<sub>2</sub>(PO<sub>4</sub>)<sub>2</sub>O<sub>2</sub>F is a commercial product (Neware), showing a reversible capacity of 104 mAh g<sup>-1</sup> and excellent stability (Figure S14). A mass ratio of 1.7:1 has been carefully adjusted to match the positive and negative capacities. Figure 5 shows the electrochemical performance of the full cell, which affords a capacity of 150 mAh g<sup>-1</sup> with an average voltage of 2.7 V. Based on the mass of cathode and anode, the specific energy is calculated to be 160 Wh kg<sup>-1</sup>. A fully charged cell can light up an LED array, thereby demonstrating its potential in practical applications (Figure S15).

## Conclusion

In conclusion, we have demonstrated the design and fabrication of TiO<sub>2</sub>(A/B) homojunction using a simple hydrothermal reaction followed by an annealing process. The composition ratio of anatase and bronze can be easily adjusted by annealing temperature and time. The TiO<sub>2</sub>(A/B) homojunction brings rich interphases and active sites for Na<sup>+</sup> storage, leading to a marked improvement in electrochemical performance. TiO<sub>2</sub>(A/B) supplies an excellent rate capability of 140 mAh g<sup>-1</sup> at 20 C and a stable capacity of 152 mAh g<sup>-1</sup> at 5 C after 3000 cycles, with a capacity decay as low as 0.005% per cycle. In addition, the full cell of TiO<sub>2</sub>(A/B)//Na<sub>3</sub>V<sub>2</sub>(PO<sub>4</sub>)<sub>2</sub>O<sub>2</sub>F exhibits specific energy of 160 Wh kg<sup>-1</sup>. This work demonstrates the potential of homojunction design in sodium batteries, which would find more applications in the engineering of electrode materials for rechargeable systems.

## Acknowledgements

This research was supported by grants from the National Natural Science Foundation of China (Grant Nos. 52172219, 51872192, 52025028, and 51772197), the Natural Science Foundation of Jiangsu Province (Grant No. BK20180002), the Natural Science Foundation of the Jiangsu Higher Education Institutions of China

(Grant No. 19KJA170001), the Priority Academic Program Development (PAPD) of Jiangsu Higher Education Institutions.

## Conflict of Interest

The authors declare no conflict of interest.

## Data Availability Statement

The data that support the findings of this study are available from the corresponding author upon reasonable request.

**Keywords:** electrochemical performance • homojunction • sodium-ion batteries • titanium dioxide

- [1] H. Y.-s. Joachim Maier, *Nat. Rev. Mater.* **2021**, *6*, 1020–1035.
- [2] J. Ni, L. Li, *Adv. Funct. Mater.* **2018**, *28*, 1704880.
- [3] Y. Jiang, Y. Wang, J. Ni, L. Li, *InfoMat* **2021**, *3*, 339–352.
- [4] R. Zhao, N. Sun, B. Xu, *Small Structures* **2021**, *2*, 2100132.
- [5] M. Huang, B. Xi, N. Shi, J. Feng, Y. Qian, D. Xue, S. Xiong, *Small Structures* **2021**, *2*, 2000085.
- [6] L. Li, Y. Xu, X. Sun, R. Chang, Y. Zhang, X. Zhang, J. Li, *Adv. Energy Mater.* **2018**, *8*, 1801064.
- [7] L. Li, Y. Xu, R. Chang, C. Wang, S. He, X. Ding, *Energy Storage Mater.* **2021**, *37*, 325–335.
- [8] W. Wang, Y. Liu, X. Wu, J. Wang, L. Fu, Y. Zhu, Y. Wu, X. Liu, *Adv. Mater. Sci. Technol.* **2018**, *3*, 1800004.
- [9] M. Mokhlesur Rahman, M. Zhou, I. Sultana, S. Mateti, A. Falin, L. H. Li, Z.-S. Wu, Y. Chen, *Batteries & Supercaps* **2019**, *2*, 160–167.
- [10] Z. Li, Y. Peng, X. Zhang, Y. Ren, W. Chen, F. Xu, N. Wang, C. Liu, L. Mo, Y. Ding, L. Hu, D. Ji, G. Cao, *Batteries & Supercaps* **2021**, *4*, 1874–1880.
- [11] J. Feng, Y. Dong, Y. Yan, W. Zhao, T. Yang, J. Zheng, Z. Li, M. Wu, *Chem. Eng. J.* **2019**, *373*, 565–571.
- [12] H. Xiong, M. D. Slater, M. Balasubramanian, C. S. Johnson, T. Rajh, *J. Phys. Chem. Lett.* **2011**, *2*, 2560–2565.
- [13] B. Chen, Y. Meng, F. Xie, F. He, C. He, K. Davey, N. Zhao, S. Z. Qiao, *Adv. Mater.* **2018**, *30*, 1804116.
- [14] H. He, Q. Gan, H. Wang, G.-L. Xu, X. Zhang, D. Huang, F. Fu, Y. Tang, K. Amine, M. Shao, *Nano Energy* **2018**, *44*, 217–227.
- [15] L. Wang, G. Yang, J. Wang, S. Wang, C. Wang, S. Peng, W. Yan, S. Ramakrishna, *Small* **2019**, *15*, 1901584.
- [16] C. Chen, Y. Wen, X. Hu, X. Ji, M. Yan, L. Mai, P. Hu, B. Shan, Y. Huang, *Nat. Commun.* **2015**, *6*, 6929.
- [17] Z. Hao, Q. Chen, W. Dai, Y. Ren, Y. Zhou, J. Yang, S. Xie, Y. Shen, J. Wu, W. Chen, G. Q. Xu, *Adv. Energy Mater.* **2020**, *10*, 1903107.
- [18] Q. Ni, R. Dong, Y. Bai, Z. Wang, H. Ren, S. Sean, F. Wu, H. Xu, C. Wu, *Energy Storage Mater.* **2020**, *25*, 903–911.
- [19] M. Fan, Z. Lin, P. Zhang, X. Ma, K. Wu, M. Liu, X. Xiong, *Adv. Energy Mater.* **2021**, *11*, 2003037.
- [20] M. Ni, D. Sun, X. Zhu, Q. Xia, Y. Zhao, L. Xue, J. Wu, C. Qiu, Q. Guo, Z. Shi, X. Liu, G. Wang, H. Xia, *Small* **2020**, *16*, 2006366.
- [21] D. Lin, Z. Lu, P.-C. Hsu, H. R. Lee, N. Liu, J. Zhao, H. Wang, C. Liu, Y. Cui, *Energy Environ. Sci.* **2015**, *8*, 2371–2376.
- [22] J. Chen, B. Luo, Q. Chen, F. Li, Y. Guo, T. Wu, P. Peng, X. Qin, G. Wu, M. Cui, L. Liu, L. Chu, B. Jiang, Y. Li, X. Gong, Y. Chai, Y. Yang, Y. Chen, W. Huang, X. Liu, M. Li, *Adv. Mater.* **2020**, *32*, e1905578.
- [23] J. Li, W. Qin, J. Xie, R. Lin, Z. Wang, L. Pan, W. Mai, *Chem. Eng. J.* **2018**, *332*, 260–266.
- [24] J. Ni, S. Fu, C. Wu, J. Maier, Y. Yu, L. Li, *Adv. Mater.* **2016**, *28*, 2259–2265.
- [25] J. Ni, S. Fu, Y. Yuan, L. Ma, Y. Jiang, L. Li, J. Lu, *Adv. Mater.* **2018**, *30*, 1704337.
- [26] J. Ni, A. Dai, Y. Yuan, L. Li, J. Lu, *Mater.* **2020**, *2*, 1366–1376.
- [27] Z. Wang, J. Ni, L. Li, J. Lu, *Cell Rep. Phys. Sci.* **2020**, *1*, 100078.
- [28] L. Wu, J. Zheng, L. Wang, X. Xiong, Y. Shao, G. Wang, J. H. Wang, S. Zhong, M. Wu, *Angew. Chem. Int. Ed.* **2019**, *58*, 811–815; *Angew. Chem.* **2019**, *131*, 821–825.
- [29] C. Hu, L. Chen, Y. J. Hu, A. P. Chen, L. Chen, H. Jiang, C. Z. Li, *Adv. Mater.* **2021**, *33*, 2103558.
- [30] Y. Li, J. Zhang, Q. Chen, X. Xia, M. Chen, *Adv. Mater.* **2021**, *33*, 2100855.
- [31] J. Ni, M. Sun, L. Li, *Adv. Mater.* **2019**, *31*, 1902603.
- [32] Y. Chen, J. Washburn, *Phys. Rev. Lett.* **1996**, *77*, 4046–4049.
- [33] X. Feng, G. Hu, J. Hu, *Nanoscale* **2011**, *3*, 2099–2117.
- [34] Lun Pan, Songbo Wang, Jiawei Xie, Li Wang, Xiangwen Zhang, J.-J. Zou, *Nano Energy* **2016**, *28*, 293–303.
- [35] G. Liu, H.-H. Wu, Q. Meng, T. Zhang, D. Sun, X. Jin, D. Guo, N. Wu, X. Liu, J.-K. Kim, *Nanoscale Horiz.* **2020**, *5*, 150–162.
- [36] G. Fang, Q. Wang, J. Zhou, Y. Lei, Z. Chen, Z. Wang, A. Pan, S. Liang, *ACS Nano* **2019**, *13*, 5635–5645.
- [37] H. Zhang, D. Li, W. J. Byun, X. Wang, T. J. Shin, H. Y. Jeong, H. Han, C. Li, J. S. Lee, *Nat. Commun.* **2020**, *11*, 4622.
- [38] S. Zhang, Z. Liu, D. Chen, Z. Guo, M. Ruan, *Chem. Eng. J.* **2020**, *395*, 125101.
- [39] S. Xiong, Z. Hou, S. Zou, X. Lu, J. Yang, T. Hao, Z. Zhou, J. Xu, Y. Zeng, W. Xiao, W. Dong, D. Li, X. Wang, Z. Hu, L. Sun, Y. Wu, X. Liu, L. Ding, Z. Sun, M. Fahlman, Q. Bao, *Joule* **2021**, *5*, 467–480.
- [40] Y.-N. Lu, J.-X. Zhong, Y. Yu, X. Chen, C.-Y. Yao, C. Zhang, M. Yang, W. Feng, Y. Jiang, Y. Tan, L. Gong, X. Wei, Y. Zhou, L. Wang, W.-Q. Wu, *Energy Environ. Sci.* **2021**, *14*, 4048–4058.
- [41] D. Su, S. Dou, G. Wang, *Chem. Mater.* **2015**, *27*, 6022–6029.
- [42] S. Lu, S. Yang, X. Hu, Z. Liang, Y. Guo, Y. Xue, H. Cui, J. Tian, *Int. J. Hydrogen Energy* **2019**, *44*, 24398–24406.
- [43] Z. Wang, Y. Wang, W. Zhang, Z. Wang, Y. Ma, X. Zhou, *J. Phys. Chem. C* **2019**, *123*, 1779–1789.
- [44] C. Chu, J. Yang, Q. Zhang, N. Wang, F. Niu, X. Xu, J. Yang, W. Fan, Y. Qian, *ACS Appl. Mater. Interfaces* **2017**, *9*, 43648–43656.
- [45] S.-T. Myung, N. Takahashi, S. Komaba, C. S. Yoon, Y.-K. Sun, K. Amine, H. Yashiro, *Adv. Funct. Mater.* **2011**, *21*, 3231–3241.
- [46] J.-Y. Shin, D. Samuelis, J. Maier, *Adv. Funct. Mater.* **2011**, *21*, 3464–3472.
- [47] T. Beuvier, M. Richard-Plouet, L. Brohan, *J. Phys. Chem. C* **2009**, *113*, 13703–13706.
- [48] J. Ni, Y. Jiang, F. Wu, J. Maier, Y. Yu, L. Li, *Adv. Funct. Mater.* **2018**, *28*, 1707179.
- [49] B. Li, B. Xi, F. Wu, H. Mao, J. Liu, J. Feng, S. Xiong, *Adv. Energy Mater.* **2019**, *9*, 1803070.
- [50] J. Y. Hwang, H. L. Du, B. N. Yun, M. G. Jeong, J. S. Kim, H. Kim, H. G. Jung, Y. K. Sun, *ACS Energy Lett.* **2019**, *4*, 494–501.
- [51] Q. Wu, J. Xu, X. Yang, F. Lu, S. He, J. Yang, H. J. Fan, M. Wu, *Adv. Energy Mater.* **2015**, *5*, 1401756.
- [52] B. Li, B. Xi, Z. Feng, Y. Lin, J. Liu, J. Feng, Y. Qian, S. Xiong, *Adv. Mater.* **2018**, *30*, 1705788.
- [53] H. Xu, Y. Liu, T. Qiang, L. Qin, J. Chen, P. Zhang, Y. Zhang, W. Zhang, W. Tian, Z. Sun, *Energy Storage Mater.* **2019**, *17*, 126–135.
- [54] C. Gao, J. Feng, J. Dai, Y. Pan, Y. Zhu, W. Wang, Y. Dong, L. Cao, L. Guan, L. Pan, H. Hu, M. Wu, *Carbon* **2019**, *153*, 372–380.
- [55] J. Li, Z. Ding, J. Li, C. Wang, L. Pan, G. Wang, *Chem. Eng. J.* **2021**, *407*, 127199.
- [56] S. ArdizzoneG, FregonaraS, Trasatti, *Electrochim. Acta* **1990**, *35*, 263–267.
- [57] L. Fang, Z. Lan, W. Guan, P. Zhou, N. Bahlawane, W. Sun, Y. Lu, C. Liang, M. Yan, Y. Jiang, *Energy Storage Mater.* **2019**, *18*, 107–113.

Manuscript received: June 12, 2022

Revised manuscript received: July 5, 2022

Accepted manuscript online: July 11, 2022

Version of record online: July 27, 2022